Journal of Marine Science and Application (2026) 25: 342-361
https://doi.org/10.1007/s11804-025-00624-5

RESEARCH ARTICLE

A Machine Learning-based Tool to Correlate Coupled and Uncoupled Numerical Simulations for Submerged Plates Subjected to Underwater Explosions

Jacopo Bardiani[1], **Luca Lomazzi**[1], **Claudio Sbarufatti**[1] **and Andrea Manes**[1]

Received: 30 November 2024 / Accepted: 31 January 2025

Abstract

In naval engineering, understanding underwater explosions is crucial for structural integrity and safety, particularly for combat ships. Coupled numerical analyses, which account for fluid-structure interaction (FSI), are accurate but computationally expensive and impractical for real-time applications. In contrast, uncoupled methods are efficient but overlook FSI effects. This study introduces a data-driven approach using a feed-forward Deep Neural Network (DNN) to estimate FSI-induced displacements from uncoupled simulations. Trained on numerical datasets of blast-loaded plates with varying characteristics, the DNN predicts the coupled displacement field based on structural parameters of uncoupled simulations. Results demonstrate that this framework provides a fast and reliable alternative to coupled simulations, offering a practical engineering tool for underwater blast scenarios. This work serves as proof of concept that deep-learning-enhanced uncoupled simulations can replace coupled ones, with validity beyond the specific structure in the case study.

Keywords Underwater explosion; Fluid-structure interaction; Numerical simulation; Deep neural network; Uncoupled approach

1 Introduction

Comprehending the dynamic behavior of submerged structures under pressure loading is crucial for the naval shipbuilding and offshore engineering sectors. Underwater explosions (UNDEX) are particularly significant among the various sources of pressure loads, as they directly impact the safety and functionality of underwater vehicles (such as submarines) and various marine structures (such as drilling platforms, cargo vessels and combat ships).

A typical UNDEX event can produce three distinct damaging mechanisms in a structure, depending on the distance from the hull (Bardiani et al., 2024; Bardiani et al., 2025; De Camargo, 2019; Ming et al., 2016; Rolfe et al., 2020; Tran et al., 2021; Zhang et al., 2018): initially, primary shock waves impact the hull with high velocity and pressure. Subsequently, pressure waves at a lower frequency, caused by the pulsation of the gas bubble generated by the UNDEX (Sagar and Moctar, 2024), excite the structure. Finally, the collapse of gas bubbles creates high-speed water jets that can strike the ship.

The previous three mechanisms induce highly complex phenomenon due to fluid structure interaction (FSI), significant deformations and fracturing phenomena, and material nonlinearity influenced by high strain rates and temperature (Liu et al., 2018; Peng et al., 2021; Rajendran and Narasimhan, 2001; Ren et al., 2022). Unlike explosions in the air, FSI induced by UNDEX events can cause several interconnected effects like cavitation, reflection and absorption.

Depending on whether the structure is within the bubble's impact zone, UNDEX can be categorized into non-contact explosions and contact explosions (Cole, 1948). Non-contact explosions can be further classified into far-field and near-field explosions, depending on the stand-off distance. For instance, in far-field UNDEX, the stand-off distance is greater than the maximum radius of the bubble formed in the first pulsation (Ming et al., 2016).

Three primary methodologies are utilized to investigate

Article Highlights

- A machine learning-based framework is developed to enhance the accuracy of uncoupled underwater explosion simulations by incorporating fluid-structure interaction effects.
- A deep neural network (DNN) is trained on numerical datasets of submerged plates subjected to blast loads, predicting coupled displacement fields from uncoupled simulations with high accuracy.
- The proposed method significantly reduces computational costs compared to fully coupled simulations, providing a fast and reliable alternative for naval and offshore engineering applications.

✉ Jacopo Bardiani
jacopo.bardiani@polimi.it

[1] Department of Mechanical Engineering, Politecnico di Milano, Via G. La Masa 120156, Milano, Italy

UNDEX and their effects: experimental tests, analytical models, and numerical simulations (Jin and Ding, 2011), focusing on both the characteristics of UNDEX loading and the nonlinear dynamic responses of structures.

Experimental investigations are challenging due to the complex and dangerous dynamic of UNDEX (Biglarkhani and Sadeghi, 2017; Cole, 1948). Moreover, the cost of such tests and the logistical difficulty make the experiments prohibitive, especially considering real-scale tests (Cui et al., 2016; Löhner et al., 2023; Yu et al., 2022). Although scaled specimens provide an effective approximation, experimental data is rarely published, limiting the understanding of UNDEX phenomena (Liu et al., 2022; Sagar and Moctar, 2023).

For what concerns analytical models, they are crucial for studying UNDEX phenomena, providing a theoretical understanding of potential effects and consequences. However, these models are primarily limited by their simplification and approximation of real-world phenomena, which may not fully capture the event's complexity (De Camargo, 2019; Kiciński and Szturomski, 2020).

For all these reasons, significant advancements in numerical methods and computing power have enabled effective numerical simulations of UNDEX events on high-performance computers (Ge et al., 2020; Nguyen et al., 2021). Advanced software such as LS-DYNA, ABAQUS, ANSYS, and MSC Dytran are extensively used to predict UNDEX transient loading and structural responses of different types of marine structures (Huang et al., 2011; Jha and Kumar, 2014; Walters et al., 2013; Wang et al., 2016).

Several numerical approaches can be employed to simulate UNDEX, but the major subdivision is represented by coupled or decoupled methodologies. Coupled methodologies resolve the interaction between the pressure wave generated by the explosion and the dynamic reaction of the ship hull within a single computational framework, facilitating simultaneous solutions (Liu et al., 2018). Uncoupled methodologies do not directly model the FSI; instead, they require two steps, addressing the fluid and structural domains sequentially (Giuliano et al., 2023).

Furthermore, the coupled numerical approaches employed to explore transient FSI issues in UNDEX contexts can be sub-classified into three primary categories depending on the strategy adopted to model fluid and structure domains (Löhner et al., 2023): Eulerian–Eulerian (E–E), Lagrangian–Lagrangian (L – L) and Eulerian–Lagrangian (E–L). The most used strategy for modelling FSI is the Coupled Eulerian-Lagrangian (CEL) technique. The CEL approach combines the strengths of Eulerian and Lagrangian theories for modelling fluid and structure, respectively, and enabling their continuous interaction (Rackwitz, 2020; Sigrist and Broc, 2023).

Although the dynamic responses of ship hulls under UNDEX loading have been extensively researched and investigated, coupled methods like CEL still present the main limit of being very computationally time-consuming (Liu et al., 2022). For instance, completing a single case study of a whole ship structure exposed to near-field UNDEX can take several days on a high-performance computer (Kong et al., 2023; Liu et al., 2022), since naval platforms are complex and large, necessitating massive Eulerian volumes to simulate the water portion around the vessel, resulting in an enormous number of cells. Also, the resolution of sophisticated algorithms to manage the interface and interaction between the two phases (Eulerian and Lagrangian) is computationally challenging (Nguyen, 2023). Thus, there is an urgent need to quickly, accurately, and economically obtain results from this type of simulation.

The integration of machine learning (ML) and artificial intelligence (AI) techniques within this framework offers a potent and innovative solution to meet this objective (Giuliano et al., 2023; Nayak et al., 2022). ML and AI methos can uncover the intricate relationships between inputs and outputs by analyzing large datasets of complex phenomena through an elaborate training process, enabling computers to automatically learn from the previous experience without being explicitly programmed (Bousmaha et al., 2022; Nguyen et al., 2019). They have been successfully applied in many fields (Hastie et al., 2009), such as computer science (Kong et al., 2023), structural and fluid mechanics (Nguyen et al., 2021), and material engineering (Lee et al., 2020). All the data needed to train machine learning algorithms are sourced from both experimental tests and numerical simulations (Neto et al., 2020; Brunton et al., 2020).

However, to date, only a few contributions have leveraged machine learning in the field of UNDEX. Liu et al. (2022) used a deep neural network (DNN) to predict the dynamic response of stiffened plates subjected to near-field UNDEX. The approach was tested against various charge masses, stand-off distances and plate thicknesses. The framework was then extended by the same authors (Ren et al., 2022), where more complex structural response and damage evolution was considered. DNNs were also leveraged to predict the structural response of stiffened cylindrical shells under far-field UNDEX, starting from the results of numerical simulations (Wang et al., 2024). A multilayer perceptron-based neural network was combined with a multiscale finite element method to predict the structural response of a coated composite cylinder subjected to near-field UNDEX (Nayak et al., 2022). Finally, a support vector machine (SVM) and a back propagation neural network were used to predict the plastic deformation and fracture area of various damaged plates (Kong et al., 2023; Liu et al., 2013).

Although previous studies have demonstrated the potential of machine learning techniques for analyzing UNDEX effects on submerged and floating marine structures, there is still a lack of tools in the literature that effectively integrate machine learning with fast uncoupled simulations to account for FSI. In this paper, we propose a novel tool that combines uncoupled simulations with machine learning to quickly and accurately predict UNDEX outcomes, while incorporating the effects of FSI.

This work has employed the idea proposed by Lomazzi et al. (2024) and has aimed to extend and enhance it in the case of underwater explosion phenomena against submerged plates, employing a more sophisticated neural network, to tackle the non-trivial nature of UNDEX with respect to air blast scenarios. Lomazzi et al. (2024) introduced a data-driven framework, aiming at accounting for FSI effects in air blast-loading scenarios assessed through uncoupled simulations and deep neural networks, specifically designed to overcome the computational limitations of coupled analyses.

Here, a DNN was trained on numerical data generated through coupled and uncoupled simulations of underwater blast-loaded plates. The DNN takes structural parameters as input from uncoupled simulations, such as out-of-plane displacement and equivalent plastic strain patterns at a specific time instant, initial mass-per-unit-area m_a values of the plate and the explosion type. The output of the DNN is represented by the out-of-plane displacement pattern correspondent to the coupled case, to account for FSI. All the simulations were carried out using the suite MSC Dytran and the proposed approach was tested against submerged fully clamped square plates. The reason for this is that submerged plates can serve as simplified representations of key structural components found in ships, such as hulls, bulkheads, and decks, which are critical to the overall integrity and safety of naval vessels. Also, the plates considered are unstiffened, focusing on the fundamental response mechanisms.

To the author's knowledge, this is the first time a detailed comparison between coupled and uncoupled approaches has been conducted for UNDEX problems, while also leveraging the significant potential of uncoupled analyses in terms of reduced computational cost.

Furthermore, this work is intended as proof of concept that uncoupled simulations enhanced by deep learning can replace coupled simulations, and the validity of the proposed method is not limited by the specific structure considered in the case study.

This paper is organized as follows: in Section 2 the entire framework is described in detail, focusing on the numerical simulations' dataset and the machine learning algorithm used. In this part, MSC Dytran numerical method is assessed against two experimental results (Kwon and Fox, 1993) and (Ramajeyathilagam and Vendhan, 2004). Section 3 provides information about the results obtained, followed by a discussion of them. The conclusions are finally summarized, highlighting advantages and drawbacks of the adopted methodology and proposing future enhancement and developments.

2 Methodology

The proposed data-driven framework for non-contact UNDEX scenarios is composed of the following steps:

1) Numerical simulations: simulations of vertical, fully clamped underwater blast-loaded plates were carried out to generate the dataset for the data-driven approach. The validation of the simulations against two experimental case scenarios are described in sections 2.1.1 and 2.1.2. Various loading conditions and plate characteristics were examined using coupled and uncoupled simulations. Specifically, two materials were considered (steel and aluminum), four types of explosions (with increasing severity), and seven different plate thicknesses, for a total of 56 combinations. The coupled method was utilized to consider FSI. A correspondent 2-step uncoupled simulation was performed for each coupled analysis without FSI effects. 2D schematic of coupled and uncoupled approaches are presented in Figure 1.

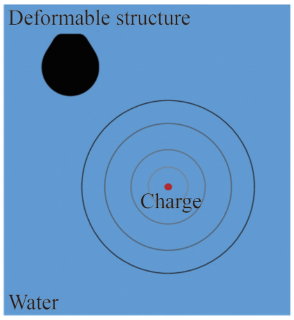

(a) CEL analysis scheme applied to the section of a submarine considering the detonation of the explosive, the wave propagation and FSI

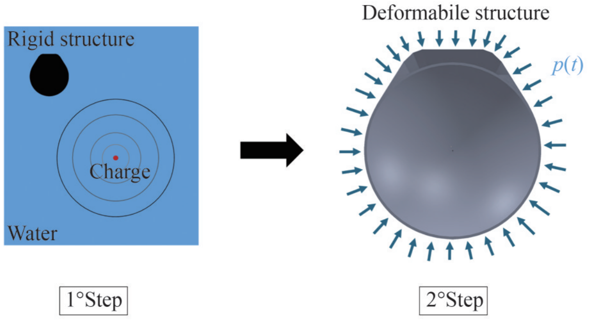

(b) UEL scheme applied to the same structure: a Eulerian simulation considers detonation of the explosive and wave propagation. The pressure is mapped and consequently applied to the structure in a Lagrangian simulation

Figure 1 Schematic representation of the CEL and UEL approach for a generic UNDEX event against a submarine

2) Dataset generation: a total of 56 coupled simulations and the corresponding 56 uncoupled simulations were performed using MSC Dytran software. All of them were post-processed in Paraview to extract the relevant data for the DNN. Data was meticulously extracted for both the fluid and the structural domains. The structural parameters considered included the plate's out-of-plane displacement, the initial mass-per-unit area, the equivalent plastic strain at the mid-surface of the plate, and the type of explosion. Additional parameters, such as structural out-of-plane velocity and the fluid overpressure, were also examined; however, none of these additional parameters contributed to improving the performance of the DNN, and they were ultimately excluded from the analysis.

3) Data-driven approach: a feed-forward DNN utilizing a back-propagation algorithm was developed to predict the plate's out-of-plane displacement field, considering FSI effects, based on the data extracted from uncoupled simulations. The DNN architecture was implemented using the PyTorch library in Python, ensuring flexibility and efficiency in the model design. Training, validation, and testing processes were conducted on the numerical dataset, following the methodology outlined below:

- Throughout training and validation, the DNN learnt how to correlate input parameters from uncoupled simulations to a displacement correction factor derived from the difference between the maximum out-of-plane displacement in uncoupled simulations and coupled simulations.
- After training, the DNN was tested against the unseen scenarios included in the testing split to verify its generalization capabilities.

Each part of the present framework is described in detail in the following subsections.

2.1 Numerical simulations

2.1.1 Validation of the numerical framework against a submerged cylinder

The framework for numerical simulations was validated against the experimental case study (Kwon and Fox, 1993). Here, a cylindrical shell submerged at 3.66 m in a pool containing an explosive charge of HBX-1. The cylindrical structure was 1.067 m long with an outer diameter of 305 mm. The wall thickness of the cylindrical part was 6.35 mm, while the endcaps were 25.40 mm thick. The cylinder was made of Aluminum T6061-T6, whose physical and material properties are shown in Table 1, the cylindrical shell possesses a density of 2 784.50 kg/m^3, an elastic modulus of 75.60 GPa and a Poisson's ratio of 0.33. It exhibits a yield stress of 300 MPa and a tensile strength of 330 MPa.

Table 1 Parameters of the Johnson-Cook model for aluminum T6061-T6

A (MPa)	B (MPa)	n (–)	C (–)	$\dot{\varepsilon}_0$ (–)
300	113.8	0.42	0.002	1.00

The charge considered in the experimental scenario was radio-controlled, was made of HBX-1 and had a mass of 27.22 kg. The explosive material was placed 7.62 m far from the outer surface of the cylinder. The schematic representation of the scenario considered is shown in Figure 2.

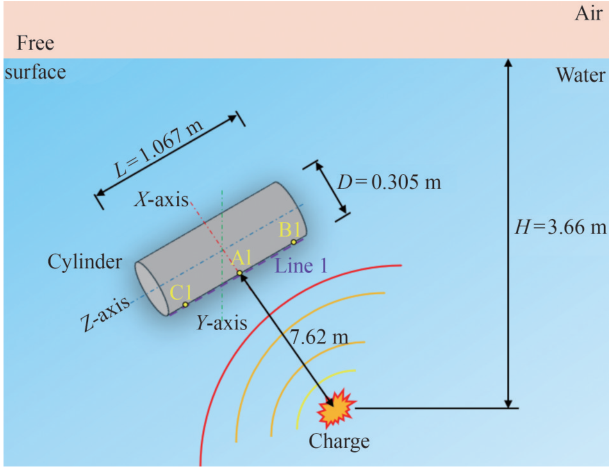

Figure 2 Schematic of the general arrangement of the experimental campaign considered for validation. A1, B1 and C1 are some of the measuring stations (Adapted from Wang et al. (2022))

Pressure sensors were installed at strategic locations to measure the peak pressure generated by the charge, the value of which was equal to 16.3 MPa with a standoff distance of 7.62 m. The sensor network installed on the structure to measure strain was composed of 14 CEA-Od 25OUW-350 strain gauges, which were bonded to the cylinder. Half the sensors measured the hoop strain, while the remaining half measured the axial strain.

MSC Dytran was used to generate the numerical model. The framework was made of two steps. First, a spherical 1D simulation was performed with a fine mesh up to the time instant at which the blast wave had almost reached the structure (Figure 3(b)). This simulation only included the fluid domain. Then, the spherical 1D solution was mapped onto a coarser 3D fluid mesh, and the structural was embedded within the fluid domain (Figure 3(a)). The second step was conducted for a total time of 0.01 s (Keil, 1961; Wang et al., 2022).

The cylinder was discretized into 2400 Lagrangian quadrilateral shell elements (CQUAD4) with a base size of 15 mm, as shown in Figure 3(c). This value was chosen based on the mesh size used in other validation studies in the literature regarding the experiment under consideration (Wang et al., 2022). Plasticity was introduced using the Johnson-Cook law, with the parameters shown in Table 1 (see Spear et al. (2021) for more details).

Thermal effects were neglected, as common practice when modeling explosive events. Furthermore, no failure model was implemented since no failure was observed in the experimental tests.

A Eulerian mesh with hexahedral elements with a base size of 8 mm is thus chosen for both the 1-D and 3-D fluid domains. This dimension was obtained through a mesh convergence analysis, reported in Figure 3(d), that ensured a good representation of the peak pressure with an affordable calculation efficiency. The 1-D model (Figure 3(a)) is

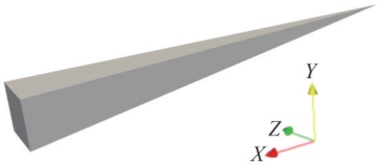

(a) 1-D spherical symmetry model

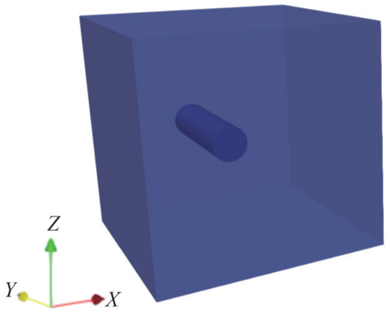

(b) 3-D model with the structure inside the Eulerian domain

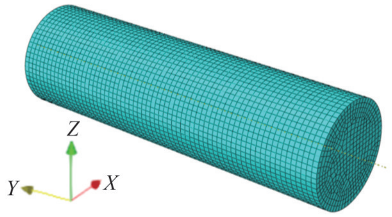

(c) Indication of the mesh used for the structure

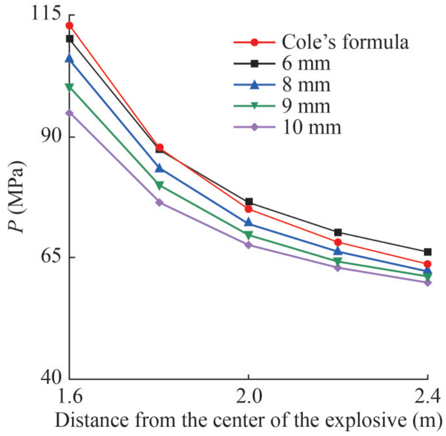

(d) Comparison of peak pressure of shock wave under different distances

Figure 3 Features of the numerical validation model

7 m long and contains both water and charge materials; the volume occupied by the charge is equal to the mass of the explosive being considered.

The 3-D model (Figure 3(b)), comprehends two distinct Euler domains to simulate the fluid both inside (air) and outside (water) the shell structure under investigation. The water 3-D domain consists of a box 2.5 m × 2.5 m × 2.5 m discretized by a hexahedral mesh. The air 3-D domain is generated with the same mesh typology.

The Jones-Wilkins-Lee (JWL) Equation of State (EOS) was adopted to describe the evolution of the charge explosion (Löhner et al., 2023; Shehu et al., 2023). This model can be expressed with the Eq. (1):

$$\begin{aligned} p = A \cdot \left(1 - \frac{\omega}{(R_1 \cdot V)}\right) \cdot e^{-R_1 \cdot V} + \\ B \cdot \left(1 - \frac{\omega}{(R_2 \cdot V)}\right) \cdot e^{-R_2 \cdot V} + \omega \cdot e/V \end{aligned} \tag{1}$$

where p, V and e are the pressure, relative volume, and relative internal energy of the detonation products respectively. A, B, R_1, R_2 and ω must be set depending on the considered charge (Shehu et al., 2023).

Instead, the polynomial equation of state (EOSPOL) was used for water (Eq. (2) and (3)). This state equation relates the pressure in the fluid to the acoustic condensation μ and the specific internal energy e. When $\mu > 0$ (compression):

$$p = a_1 \cdot \mu + a_2 \cdot \mu^2 + a_3 \cdot \mu^3 + \left(b_0 + b_1 \cdot \mu + b_2 \cdot \mu^2\right) \cdot \rho_0 \cdot e \tag{2}$$

While for $\mu < 0$ (tension):

$$p = a_1 \cdot \mu + \left(b_0 + b_1 \cdot \mu\right) \cdot \rho_0 \cdot e \tag{3}$$

where p is the pressure, $\mu = \eta - 1$, $\eta = \rho/\rho_0$, ρ_0 is the reference density, ρ is the whole material density, a_1, a_2, a_3, b_0, b_1 and b_2 are eulerian fluid constants. Finally, e represents del specific internal energy per unit mass. The gamma law (EOSGAM) used for the air inside the cylinder was a gamma law gas model (Wang et al., 2016), as expressed by Eq. (4). In fact, the gamma law gas model describes the behavior of a gas under varying conditions based on the ideal gas law, where the specific heat ratio (γ) is assumed constant (Olmi and Nascimento, 1999).

$$p = \left(\gamma - 1\right) \cdot \rho \cdot e \tag{4}$$

where ρ is the density, γ the heat capacity, and e the specific internal energy.

All the properties of the fluid domain used in the numerical model are reported in Table 2.

Hydrostatic pressure was initialized by the HYDRSTAT entry, and the boundaries of the 1D and 3D models were assigned non-reflecting boundary conditions.

The results for the 1D and 3D models are reported in Figure 4 for two representative time instants. The experimental observations obtained by the strain gauges installed at position B1were considered for validating the numerical model.

Table 2 Material properties of the fluid domain for the numerical model for validation

Material	MSC Dytran model	Input parameters
Water	Polynomial equation of state (EOSPOL)	$\rho = 1\,025$ (kg/m^3), $K = 2.2\cdot10^9$ (Pa), $e = 83\,950$ (J/kg), $a_1 = 2.314\cdot10^9$ (Pa), $a_2 = 6.561\cdot10^9$ (Pa), $a_3 = 1.126\cdot10^9$ (Pa), $b_0 = 0.4934$ (–), $b_1 = 1.3937$ (–), $b_2 = 0.00$ (–)
Charge (HBX-1)	JWL equation of state (EOSJWL)	$\rho = 1\,720$ (kg/m^3), $W = 27.00$ (kg), $e = 5.60\cdot10^6$ (kJ/kg), $A = 5.32\cdot10^{11}$ (–), $B = 7.13\cdot10^9$ (–), $R_1 = 4.15$ (–), $R_2 = 0.95$ (–), $\omega = 0.3$ (–)
Air inside the cylinder	Gamma law (EOSGAM)	$\rho = 1.225$ (kg/m^3), $\gamma = 1.4$ (–), $e = 2.14\cdot10^5$ (J/kg), $R = 287\left(\frac{\text{J}}{\text{kg}\cdot\text{K}}\right)$

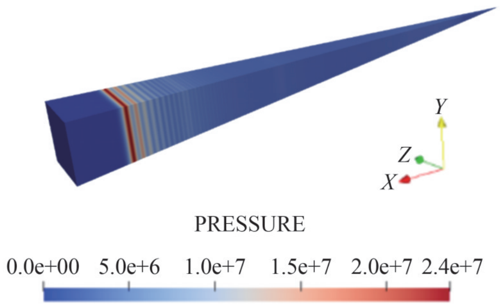

(a) $t = 0.0045$ s

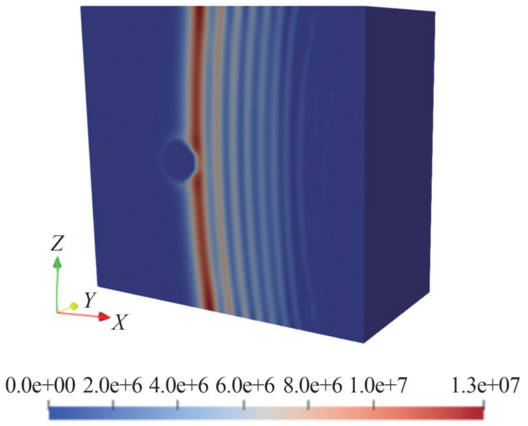

(b) $t = 0.0065$ s

Figure 4 Pressure field at different instants for the 1D and 3D models (in Pa)

The numerical results are compared to the experimental data in Figure 5(a) and (b). Here, time 0 ms identifies the time at which the strain gauges start to measure non-null values. Also, Figure 5(c) presents the comparison of numerical and experimental pressure-time curve, showing an accurate correspondence.

The two sets of curves regarding the strain trend exhibited an initial peak followed by a significant amplitude decline and several fluctuations. Overall, the numerical model was able to accurately match the experimental strain measurements.

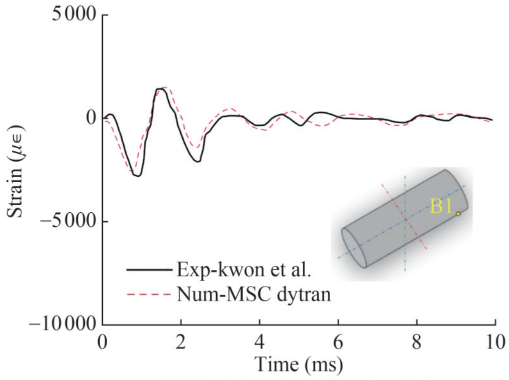

(a) Axial strain at location B1

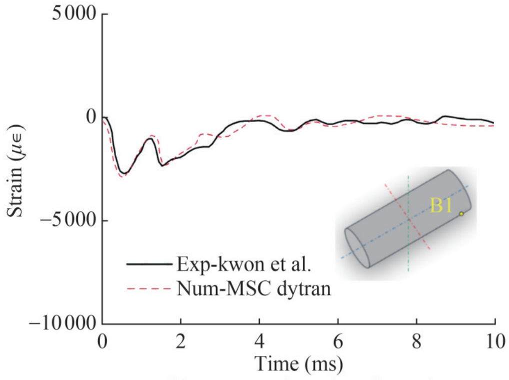

(b) Hoop strain at location B1

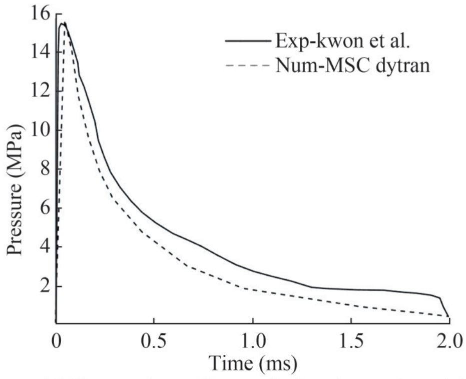

(c) Comparison of numerical and experimental pressure-time curve

Figure 5 Comparison of experimental and numerical observations

2.1.2 Validation of the numerical framework against a horizontal plate

Additionally, a second experimental case from the literature has been considered to further demonstrate the validity of the results obtained with MSC Dytran. In particular, the experimental investigation proposed by Ramajeyathilagam and Vendhan (2004) is considered where rectangular unstiffened steel plates with an exposed area of 0.30 × 0.25 m^2 were subjected to underwater shock. To avoid overburdening the discussion, only a comparison of the numerical and experimental results is presented in Figure 6, highlighting a good agreement. For further details on the experimental trial, refer to. The mesh size considered in the present model is 5 mm (Ramajeyathilagam and Vendhan, 2004).

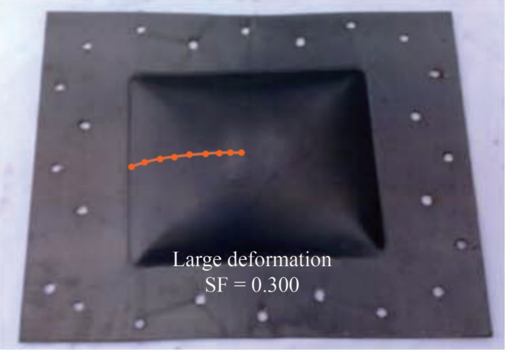

(a) Experimental plate

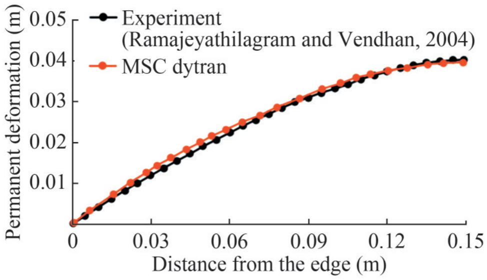

(b) Comparison between numerical and experimental

Figure 6 Features of the experimental plate and results

2.1.3 Numerical simulations of the dataset

All numerical simulations in the dataset were based on the code MSC Dytran version 2023.3 in an explicit framework. MSC Dytran is an explicit finite element analysis (FEA) solution for the simulation of short-lived events, such as shocks and collisions, and for the analysis of the complex nonlinear behavior that structures undergo during these events. The accuracy of the results provided by the software in the case of underwater explosion scenarios was already proven in Section 2, where an experimental case of UNDEX against a cylinder was replicated numerically. MSC Patran version 2023.3 was used to discretize geometries and generate meshes (both structural and Eulerian). Vertical fully clamped metal plates, made by aluminum and steel, were simulated against underwater explosion loadings according to the schematic representation presented in Figure 7. The plates considered are flat, focusing on the fundamental response mechanisms.

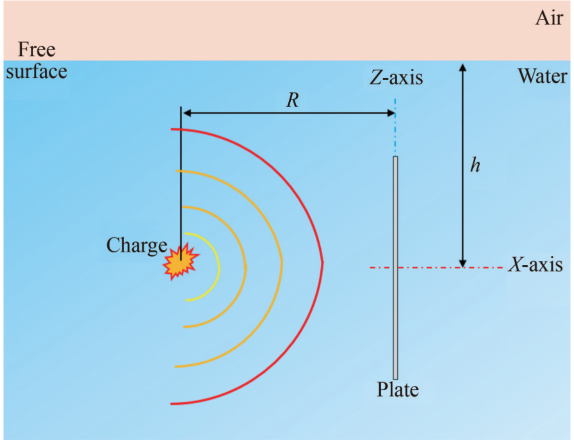

Figure 7 Scenario considered: relative position between structure and charge

All squared plates have an exposed area of 500 mm × 500 mm, with different thicknesses. The geometric center of the vertical plates has been fixed 2 meters below the free surface (dimension *h* in Figure 7).

Several UNDEX scenarios were simulated, based on different masses of the TNT charge, materials and thicknesses of the structure. Table 3 provides information about all numerical simulations performed, with a specific alphanumeric code (each case involves the coupled analysis, and the correspondent 2-step uncoupled one). The location of the charge in all explosion scenarios was *R* equal to 0.5 m laterally with respect to the geometric center of the plates (Figure 7). The mass-per-unit areas m_a (product between the density and thickness of the plate) and all the explosion load cases are reported in Table 4 and Table 5, respectively. Both steel and aluminum plates have been considered, since they are the most used in the naval sector (DNV, 2015). The physical properties of the two materials considered are shown in Table 6. Also in this case, JWL model is used to describe the evolution of the TNT charge explosion, with the parameters taken from (Shehu et al., 2023).

MSC Dytran offers two methods to simulate all the explosion scenarios. The first method, general coupling, can be applied to non-orthogonal Euler meshes but it is computationally expensive. The second method, called fast coupling, requires the Euler mesh to be orthogonal and considerably faster. This makes the fast-coupling approach the most used method. An important concept within Dytran is the definition of the coupling surface when using approaches with a Eulerian and Lagrangian part (like in the present one). The coupling surface defines what part of the Euler domain is covered by the structure. Therefore, it must be a closed volume, to separate the fluid domain from the structure domain. On many occasions, this requirement is satis-

Table 3 Codes for all the cases considered in the dataset

Case	Code	Case	Code	Case	Code
1	AL1-T1-LC1	20	AL1-T5-LC4	39	ST1-T10-LC3
2	AL1-T1-LC2	21	AL1-T6-LC1	40	ST1-T10-LC4
3	AL1-T1-LC3	22	AL1-T6-LC2	41	ST1-T11-LC1
4	AL1-T1-LC4	23	AL1-T6-LC3	42	ST1-T11-LC2
5	AL1-T2-LC1	24	AL1-T6-LC4	43	ST1-T11-LC3
6	AL1-T2-LC2	25	AL1-T7-LC1	44	ST1-T11-LC4
7	AL1-T2-LC3	26	AL1-T7-LC2	45	ST1-T12-LC1
8	AL1-T2-LC4	27	AL1-T7-LC3	46	ST1-T12-LC2
9	AL1-T3-LC1	28	AL1-T7-LC4	47	ST1-T12-LC3
10	AL1-T3-LC2	29	ST1-T8-LC1	48	ST1-T12-LC4
11	AL1-T3-LC3	30	ST1-T8-LC2	49	ST1-T13-LC1
12	AL1-T3-LC4	31	ST1-T8-LC3	50	ST1-T13-LC2
13	AL1-T4-LC1	32	ST1-T8-LC4	51	ST1-T13-LC3
14	AL1-T4-LC2	33	ST1-T9-LC1	52	ST1-T13-LC4
15	AL1-T4-LC3	34	ST1-T9-LC2	53	ST1-T14-LC1
16	AL1-T4-LC4	35	ST1-T9-LC3	54	ST1-T14-LC2
17	AL1-T5-LC1	36	ST1-T9-LC4	55	ST1-T14-LC3
18	AL1-T5-LC2	37	ST1-T10-LC1	56	ST1-T14-LC4
19	AL1-T5-LC3	38	ST1-T10-LC2		

Table 4 Mass-per-unit-area m_a of all the plates in the dataset

Thickness code	ρ (kg/m^3)	s (m)	m_a (kg/m^2)
T1	2 700	0.008	21.6
T2	2 700	0.012	32.4
T3	2 700	0.016	43.2
T4	2 700	0.020	54.0
T5	2 700	0.024	64.8
T6	2 700	0.028	75.6
T7	2 700	0.032	86.4
T8	7 850	0.008	62.8
T9	7 850	0.012	94.2
T10	7 850	0.016	125.6
T11	7 850	0.020	157.0
T12	7 850	0.024	188.4
T13	7 850	0.028	219.8
T14	7 850	0.032	251.2

Table 5 Features of the explosion scenarios considered

Case	Code	Charge	m (kg)	EOS	R_{charge} (m)	R (m)	HSF (–)
1	LC1	TNT	0.30	JWL	0.035	0.5	1.10
2	LC2	TNT	0.15	JWL	0.028	0.5	0.77
3	LC3	TNT	0.10	JWL	0.025	0.5	0.63
4	LC4	TNT	0.05	JWL	0.020	0.5	0.43

fied, but some issues emerge when the object of the investigation is a plate modelled with shell elements. In this case, the meaning of the coupling surface must be changed. The coupling surface will no longer act as a container of fluid but will only act as a barrier to fluid flow. This new approach is called "auto-coupling", and it's activated by using PARAM and AUTOCOUP in the input file of the analysis settings. The latter represents the technology used in the present study since it's the preferred choice for plate structures. The software uses a specific FSI algorithm to couple both Lagrangian and Eulerian domains.

The Lagrangian domain (structure) was described using shell 3 844 elements CQUAD4 with an average mesh of 8 mm. These elements are quadrilateral shell elements with four grid points, using Key-Hoff formulation due to its great efficiency. Some tests were performed to choose the best formulation: although Belytschko-Tsay is the most efficient and should be used in most situations, the Key-Hoff one is more expensive, but performs better at large strains.

As in the validation paragraph, all materials considered are governed by the von Mises criterion, according to the Johnson-Cook plasticity model (Murugesan and Jung, 2019). Table 7 reports all the parameters considered for the two materials.

For a complete high-fidelity representation of the progressive damage of the structure under the underwater blast event, structural damage behavior was considered, using the Johnson-Cook failure model, through a subroutine. It defines the properties of a failure model where failure is determined by a damage model. The damage model is given by the following Eq. (5):

Table 6 Physical constants of the plate materials used in the numerical simulations

Material	E (GPa)	ν (–)	ρ (kg/m^3)	c_p (J/kgK)	χ (–)	T_r (K)	T_m (K)
Steel alloy (ST)	210.0	0.33	7 850	452	0.9	293	1 800
Aluminum alloy (AL)	70.0	0.30	2 700	910	0.9	293	893

Table 7 Material parameters of the plate materials used in the numerical simulations

Alloy	Code	A (MPa)	B (MPa)	n (–)	C (–)	$\dot{\varepsilon}_0$ (–)	m (–)	Ref.
6061-T6	AL1	270.0	154.30	0.221	0.130	1.0	1.34	Venkatesan et al., 2017
AISI-316L	ST1	490.0	600.00	0.210	0.015	1.0	0.60	Elkaseer et al., 2019

$$\varepsilon_{\text{frac}} = \left[D_1 + D_2 \cdot e^{D_3 \cdot \sigma^*}\right] \cdot \left[1 + D_4 \cdot \ln\left(\frac{\dot{\varepsilon}_{pl}}{\dot{\varepsilon}^0_{pl}}\right)\right] \cdot \left[1 + D_5 \cdot \frac{T - T_{\text{room}}}{T_{\text{melt}} - T_{\text{room}}}\right] \qquad \sigma^* = \frac{p}{\bar{q}} \tag{5}$$

where $\varepsilon_{\text{frac}}$ is the equivalent strain to fracture under the present conditions of stress, strain rate and temperature, $D_1 - D_5$ are failure parameters, p is the mean (or hydrostatic) stress, q is the von Mises stress, $\dot{\varepsilon}^0_{pl}$ is the reference strain rate, $\dot{\varepsilon}^{pl}_e$ is the plastic strain rate, T is the current analysis temperature, T_{room} is the reference temperature and finally T_{melt} is the melting temperature. In this study, the effect of temperature on structure response was suppressed (by setting $D_5 = 0$) is a typical assumption (Ding and Buijk, 2006; Shehu et al., 2023).

The damage of an element D is defined based on a cumulative damage law, and it can be represented in a linear way as shown in Eq. (6) (Murugesan and Jung, 2019):

$$D = \sum_{\text{time}} \frac{\Delta\varepsilon_p}{\varepsilon_{\text{frac}}} \tag{6}$$

where $\Delta\varepsilon_p$ is the equivalent plastic strain increment. The summation is performed over all past time increments. The damage of an element is defined based on a cumulative damage law, and it can be represented linearly with Eq. (7):

$$\sigma_D = \sigma_{\text{eq}} \cdot (1 - D) \tag{7}$$

where σ_D is the damaged stress state and D is the damage parameter, the latter varying between 0 and 1. Furthermore, the equivalent stress σ_{eq} can be obtained from undamaged material, considering the plastic's behavior until the necking formation (Murugesan and Jung, 2019). The values of the parameters of Johnson–Cook damage model for the materials used are reported in Table 8.

The fluid domain (only water, since air is not considered for simplicity) underwent discretization employing cell-centred finite volumes (CCFV), which are advantageous for forecasting discontinuities arising from the shock wave. This aligns with the Eulerian formulation, wherein the mesh remained stationary while the fluid traversed. A sufficiently large, fixed box defines the domain's boundary using the MESH, BOX option. The fluid mesh used for this domain consists of elements with the dimensions 2.0 m × 2.0 m × 2.0 m. This fluid water block was meshed with approximately 200 × 200 × 200 hexahedron elements for each side. This mesh dimension ensures a good accuracy of the peak pressure generated by the explosion scenario (Cole, 1948), as already mentioned in section 2.1.1. The numerical model described above is shown in Figure 8, with a clear indication of the Lagrangian mesh, with its center of gravity located exactly in the middle of the fluid domain.

A resume of all material properties used in the present simulations, with the related model used in MSC Dytran, is reported in Table 9.

As already discussed, hydrostatic pressure significantly impacts the bubble pulse, although it is negligible compared to the immense pressure of the shock wave. Therefore, hydrostatic pressure must be accounted for in numerical simulations to represent the structural response better. All boundary conditions for the outer mesh of the 3-D model were given a flow non-reflecting boundary. The non-reflecting boundary condition should effectively

Table 8 Identification of the parameters of the steel and aluminum used within the Johnson-Cook failure model

Mat.	D_1 (MPa)	D_2 (MPa)	D_3 (–)	D_4 (–)	D_5 (–)	$\dot{\varepsilon}^0_{\text{pl}}$ (–)	Ref.
Steel	0.025	16.930	−14.80	0.0214	0	1.0	Murugesan and Jung, 2019
Alum.	0.096	0.049	−3.46	0.0160	0	1.0	Flores-Johnson et al., 2014

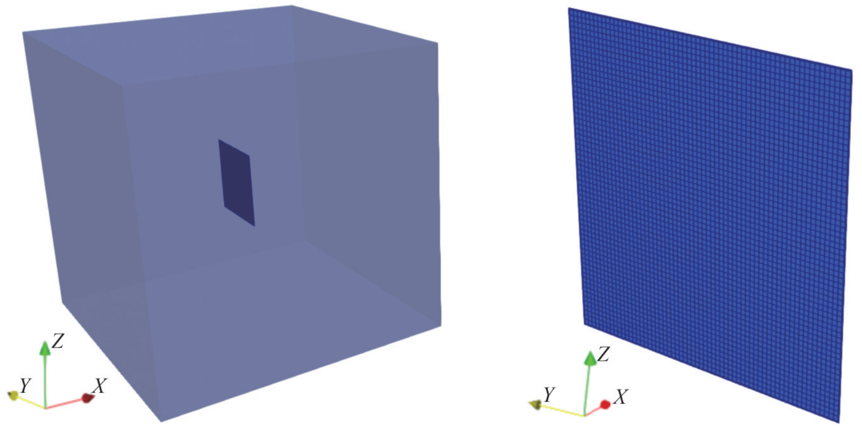

(a) 3-D numerical model considered for the UNDEX (b) Fully clamped plate with its mesh

Figure 8 Features of the numerical model implemented in MSC Dytran

Table 9 Resume of the eulerian material properties (water and charge) for all the simulation in the dataset

Material	MSC Dytran model	Input parameters
Water	Polynomial equation of state (EOSPOL)	Same as Table 2
Charge (TNT)	JWL equation of state (EOSJWL)	$\rho = 1\,630$ (kg/m^3), $\gamma = 1.4$ (–), W = See Table 5, $e = 4.76 \cdot 10^6$ (kJ/kg), $A = 3.7 \cdot 10^{11}$ (–), $B = 2.23 \cdot 10^9$ (–), $R_1 = 4.15$ (–), $R_2 = 0.95$ (–), $\omega = 0.3$ (–)

absorb the outward pressure wave to avoid spurious reflection [54].

In Table 5, as already mentioned, R represents the standoff distance between the center of mass of the charge and the center of the charge plate and *HSF* the Hull Shock factor is a typical index of explosion severity about damage to hull structures (external planking) (Ming et al., 2016). To calculate this value, Eq. (8) is commonly employed (Lee et al., 2008):

$$\mathrm{HSF} = \frac{\sqrt{W_{\mathrm{TNT}}}}{R} \tag{8}$$

where W_{TNT} is the TNT equivalent weight of the charge in kg and R was already defined above. This is not the only way to define the severity of the shock, but for the simple plate under investigation it's sufficient. The total time for all analyses is set to 0.002 seconds, based on the time where the plates show the maximum deformations, and it took about 30 hours to finish one case coupled case. This number of hours indeed proves the great limitation of coupled techniques, although we are dealing with a simple plate.

All the previous information is specifically for coupled simulations, so with FSI effects. A total of 56 coupled scenarios have been considered. The same quantities of numerical simulations have been conducted in an uncoupled framework, through the application of a 2-step procedure as follows (see more details in Hinton et al. (2006)):

- Numerical simulations like the one presented so far, but with the structure rigid, so not deformable and without any motions (MATRIG entry in MDC Dytran). Starting from the results obtained on the rigid structure, the pressure over time for all mesh elements is extracted and stored.
- The pressure extracted in the first step is applied to each element of the mesh element, with the same boundary conditions as described above (fully clamps applied to all boundary edges of the plates) and without the presence of the fluid domain, so in a pure Lagrangian transient analysis.

In the present case, the first step of the uncoupled approach is consistently much faster (a quarter of time) than the coupled analysis since the structure is rigid and no FSI algorithm should be applied. Here, the pressure to be applied on the plate for the second step is calculated through a numerical simulation, but analytical formulation or experimental data could be used for enhancing the time's performance of the proposed method. The time required for the second step of the uncoupled framework is approximately a few seconds. The previous time calculation was performed by averaging the times obtained from the analyses conducted on the dataset.

The difference between coupled and uncoupled results, for what concerns the pressure field distribution in the fluid domain and full field of displacement at the instant of maximum deformed configuration (case AL1-T1-LC1 of Table 3), is presented in Figures 9 and 10, respectively. Figure 9 presents a vertical central cut in the Eulerian domain, to visualize better the results. All the results of the other analysis within the dataset are not reported, for simplicity of exposition, but they all have qualitatively similar patterns. Referring for simplicity to the maximum displacements accrued by the plate (Figure 10), it can be observed that the results of the uncoupled case (Figure 10(b) and (d)) are much more severe than the corresponding coupled case (Figure 10(a) and (c)). The same behavior is observed in all analyses, i.e. that FSI reduces the effects in terms of displacement in the case of underwater explosions. The same effect, but much less pronounced, was shown in (Giuliano et al., 2023; Lomazzi et al., 2024) in the case of air blast plates. Finally, as expected, the maximum deformations of the plates, for the coupled and uncoupled case, occur at different time instants.

2.2 Dataset generation

The numerical simulations were post-processed using Paraview scripts to extract the data required for the DNN. Post-processing operations involved extracting the following quantities for each simulation:

- Out-of-plane displacement time history $d(t)$ for each finite element of the vertical plate;
- Equivalent plastic strain time history $\varepsilon_{pl}(t)$ of the mid-surface of each element;
- Initial mass-per-unit-area m_a values were calculated according to the following equation:

$$m_a = \rho \cdot s \tag{9}$$

where ρ is the material density and s is the plate thickness. All the initial m_a values have already been presented in Table 4 and they are considered for simplicity constant during each analysis. Type of explosive scenario, according to the four categories presented in Table 5.

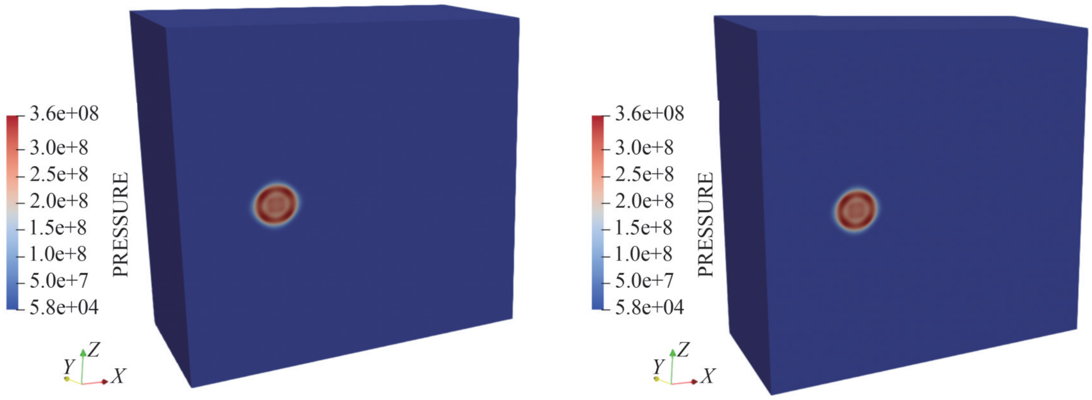

(a) $t = 0.000\,05$ s (Coupled case)

(b) $t = 0.000\,05$ s (Uncoupled case)

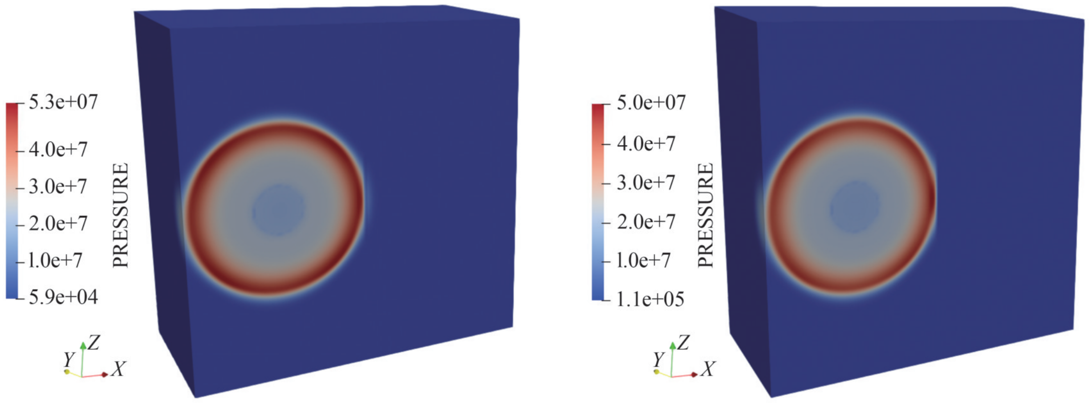

(c) $t = 0.000\,3$ s (Coupled case)

(d) $t = 0.000\,3$ s (Uncoupled case)

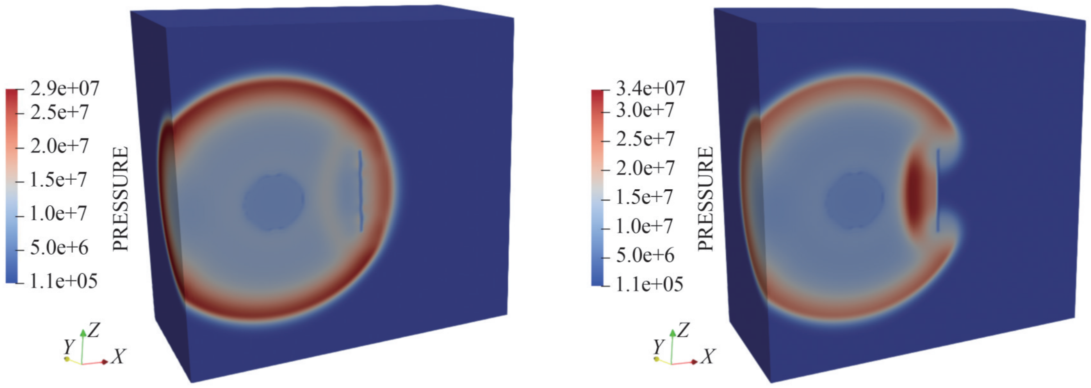

(e) $t = 0.000\,5$ s (Coupled case)

(f) $t = 0.000\,5$ s (Uncoupled case)

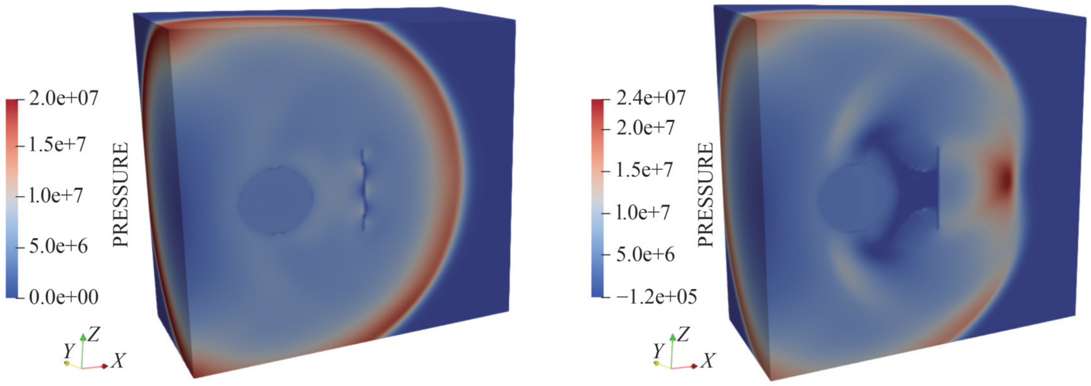

(g) $t = 0.000\,7$ s (Coupled case)

(h) $t = 0.000\,7$ s (Uncoupled case)

Figure 9 Pressure field at different instants for the 3-D model (in Pa) for a representative coupled and uncoupled cases

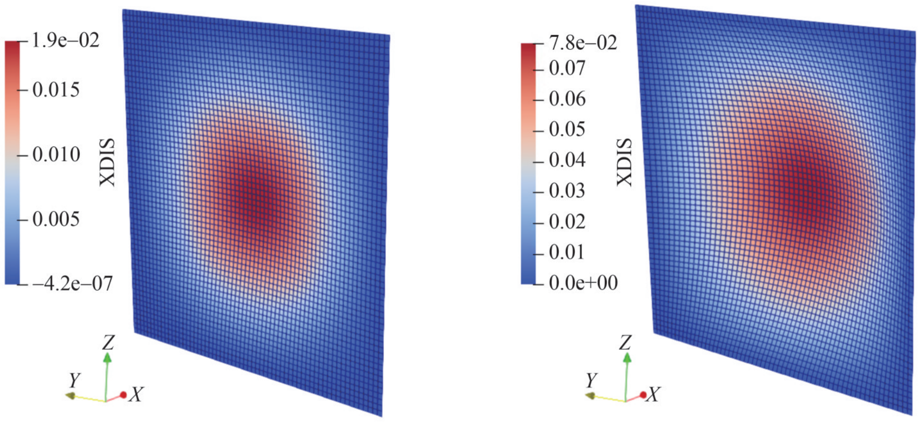

(a) $t = 0.0011$ s (Coupled case, 3-D view) (b) $t = 0.0008$ s (Uncoupled case, 3-D view)

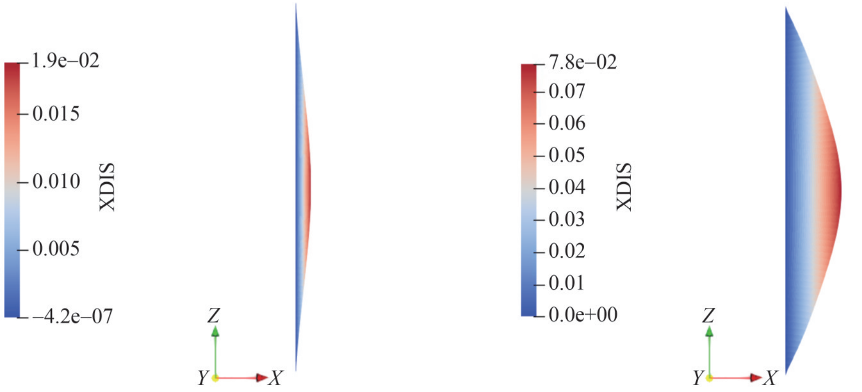

(c) $t = 0.0011$ s (Coupled case, lateral view) (d) $t = 0.0008$ s (Coupled case, lateral view)

Figure 10 Displacement distribution contour (in m) for different views

The previous time histories ($d(t)$ and $\varepsilon_{pl}(t)$) were further processed to distil the minimal amount of relevant information. For each plate, the displacement-time history of each element of the mesh was reduced to a single value, d^p, extracted at the time instant t_d when the plate center experienced maximum displacement. At the same time instant t_d was also used to extract the equivalent plastic strain of the mid-surface of each element.

The choice of extracting $\varepsilon_{pl}(t)$ was guided by the great difference in the displacement fields between coupled and uncoupled cases. In fact, uncoupled simulations mature much greater out-of-plane deformations than the coupled counterpart, making it probable that areas enter in the plastic field.

Velocity and pressure time histories were also extracted, as suggested by Lomazzi et al. (2024) and reduced to single-valued indicators. These indicators were identified as the maximum velocity over time v^p of each plate element, and the peak overpressure p^p exerted on it (Figure 11). Unlike the case of displacement, the maximum pressure and velocity peaks are recorded at different instants, due to the spherical propagation of the primary shock. The DNNs trained considering velocity and pressure also did not show significantly improved performance. Hence, such information was considered not relevant to UNDEX and was discarded from the dataset.

Representative extracted features are shown in Figure 11 in reference to simulation AL1-T1-LC1 (Table 3). Despite the cases examined being classified as underwater contact explosions, the influence of the gas bubble can be considered negligible, as it does not alter the features extracted from the numerical simulations. This is clear if observing the last plot within Figure 11, where the instant of contact between the bubble and the plates is highlighted. Also, it has been demonstrated through Cole's formulation that the gas bubbles don't pulse, since they reach the free surface before the first cycle of pulsation.

Each scenario was represented by 6 features, in particular, some vectors, including of d_U^p, d_C^p, $\varepsilon_{pl,U}^p$ and $\varepsilon_{pl,C}^p$, then the type of explosion as a categorical feature, and finally the value of m_a. The input vectors d_U^p, d_C^p, $\varepsilon_{pl,U}^p$ and $\varepsilon_{pl,C}^p$ contain in each position the respective value for a specific mesh element. To improve the effectiveness of the machine learning model, the explosion type was considered as categorical input feature, through the application of embedding technique. A total number of four explosion types have been considered and described in Table 5. Embedding works in three phases: i) initialization, where embedding vectors are initially randomly assigned, ii) training, during which embedding vectors are updated, along with the

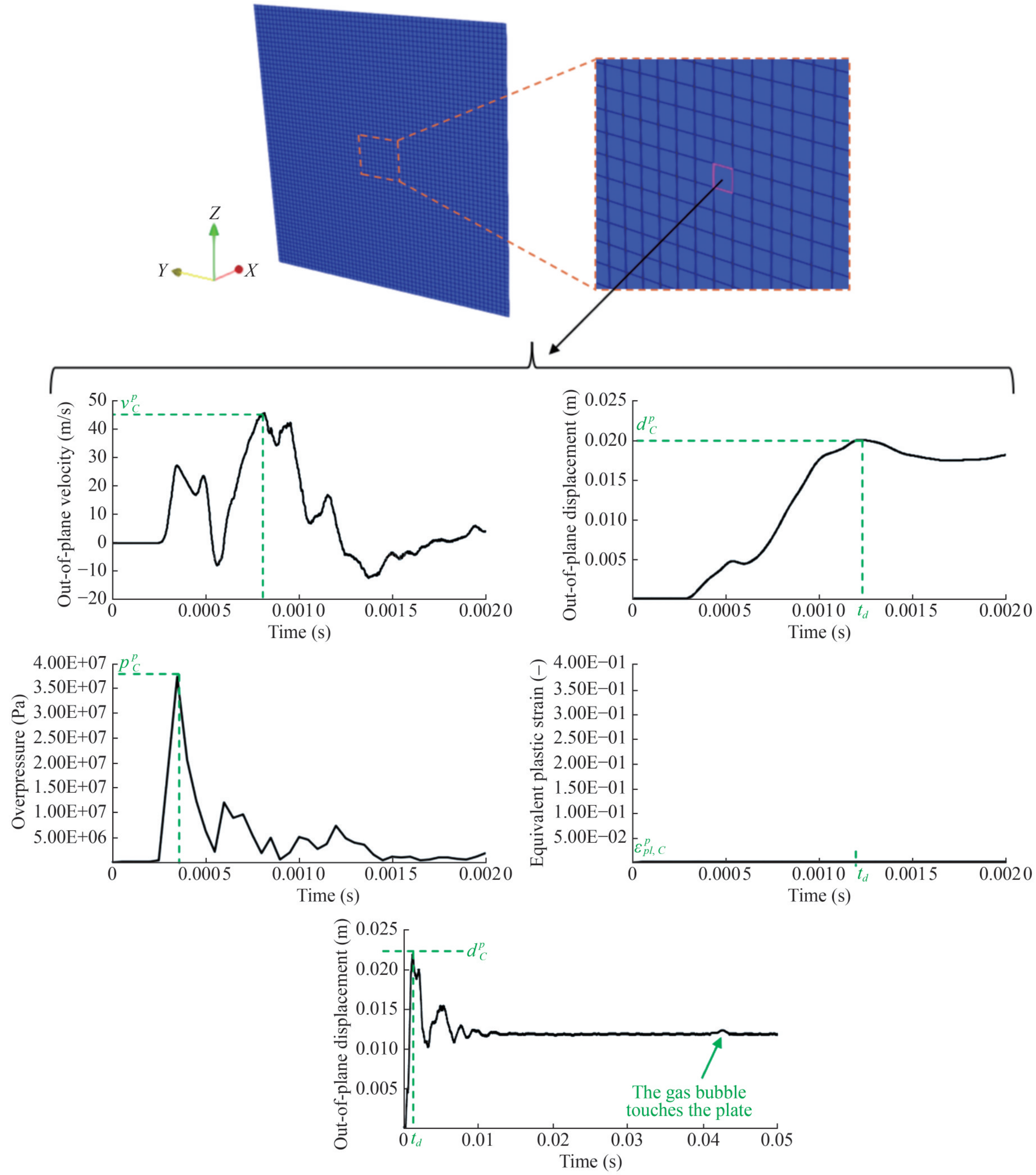

Figure 11 Illustration of the post-processing procedure made by ParaView for the AL1-T1-LC1 scenario (coupled), applied to a generic mesh element (the central one of the plates). Out-of-plane velocity and overpressure have not been considered as input to the DNN

model weights to minimize a loss function, and iii) usage, which consists of using the embedding vectors as inputs. Embedding was employed due to its numerous advantages, among which the possibility of capturing semantic relationships between categories is worth mentioning (Kumar et al., 2023).

Data augmentation was used to increase the amount of data available for training, without collecting new data (Mumuni and Mumuni, 2022). During such a process, new training examples were generated, and the essential characteristics of the original data were retained. Specifically, the strain and displacement fields provided by the numerical simulations were rotated by three different angles. Furthermore, each field was flipped with respect to the vertical z-axis shown in Figure 11. Data augmentation allowed increasing the dataset size from 56 scenarios to 448 scenarios. This number of samples was determined through an initial analysis, which indicated that this number was sufficient to achieve stable and accurate results for the specific problem addressed.

The training data of all 448 cases were randomly divided into three groups: 70% for training (304 samples), 20% for validation (76 samples) and 15% for testing (14 samples), as commonly done in neural network applications (Zhou, 2021). Furthermore, input and output data were normalized in the same way prescribed in (Lomazzi et al., 2024).

2.3 Data-driven approach

Neural networks (NNs) are models commonly employed to approximate linear and/or non-linear functions of the form $\boldsymbol{y} = f(\boldsymbol{x})$ between input $(\boldsymbol{x})$ and output $(\boldsymbol{y})$ vectors. NNs consist of interconnected units known as neurons (or nodes), organized into multiple layers: an input layer, one or more hidden layers and an output layer. NNs that contain more than one hidden layer are referred to as DNNs. This machine learning technique is inspired by the learning mechanisms of the human brain, advanced by Hinton et al. (2006).

Typically, neurons in consecutive layers are fully connected, meaning that each node in a layer is linked to all the nodes in the subsequent layer.

The i-th component x_i of the input vector $(\boldsymbol{x})$ is assigned to the i-th neuron within the input layer, which transfers information to neuron j in the subsequent layer through a weighted connection characterized by weight w_{ij}. The information obtained by the j-th node is then aggregated and updated according to the following Eq. (11) (Zhou, 2021):

$$z_j = g\left(\sum_{i=1}^{N_j}\left(w_{ij} \cdot x_i\right) + b_j\right) \tag{10}$$

where z_j is the output of the j-th node, $g(\cdot)$ is a typically non-linear activation function, N_j represents the number of nodes from which the j-th node receives information, and b_j is a bias parameter. This message passing and aggregation process recurs layer-by-layer until the output layer, where the value of the k-th node corresponds to the k-th component $\left(\hat{y}_k\right)$ of the estimated output vector $(\hat{\boldsymbol{y}})$. Weights w_{ij} and biases b_j are trainable parameters of the NN and are optimized during training through error back-propagation algorithms with gradient descent, aimed at minimizing the discrepancy between the expected output $(\boldsymbol{y})$ and the predicted output $(\hat{\boldsymbol{y}})$.

The training set is used to make the NN learn the relationship between inputs and outputs, the validation set serves as a tool to indicate underfitting or overfitting, while the testing set is used after training for evaluating the NN generalization capabilities on unseen data. Across epochs, a user-defined error metric comparing predicted and expected outputs guides the iterative update of trainable parameters using gradient descent, culminating in achieving satisfactory reconstruction error (Zhou, 2021).

Various DNNs architectures were explored in this work. However, in the interest of brevity, only the best performing configuration is presented below. The schematic diagram of the DNN implemented in the present work is shown in Figure 12.

In this work, input data consisted of two vectors (d_U^p and $\varepsilon_{pl,U}^p$), a single value correspondent to the initial m_a and finally an embedding layer for the explosion type. All the input data are then passed through the hidden layers, characterized by the following configuration. Each input is connected to different fully connected layers, with appropriate dimensions. The previous four dense layers are then concatenated and passed to a dropout layer, which helps prevent overfitting by randomly deactivating some nodes during training. The information is then passed to the output layer, which outputs the prediction of the plate displacement accounting for FSI. A total of six hidden layers were used, each one containing 400 neurons, motivated by the need to capture the complexity of non-linear relationships in the data.

Among the several activation functions that were tested during training, i.e., rectified linear unit (ReLU), sigmoid, softmax, and tanh, the ReLU activation function provided the best performance. Thus, in this work, all the nodes in the hidden layers employed the ReLU activation function, while the output nodes produced the result through a linear activation function.

Training was performed by employing the Adam optimizer using a batch size equal to 32, learning rate = 1×10^{-5}, $\beta_1 = 0.9$, $\beta_2 = 0.999$ and $\epsilon = 1 \times 10^{-7}$. The mean squared error (MSE) loss function was employed. Metrics were tracked during the training process, with an early stopping criterion set to trigger if the validation loss did not decrease for 100 consecutive epochs. Training was terminated either according to the early stopping criterion and in particular the model weights were reverted to those from the epoch that had the best validation loss within the last 100 epochs.

3 Results and discussion

The performance of the DNN over the training and test sets is shown in Figures 13 and 14, respectively. For the training set, two representative cases are shown, while for the test set, eight cases are displayed. In the interest of clarity, Figures 13 and 15 show the out-of-plane displacement over the plate's horizontal cross-section. The results brought evidence that the network successfully learnt to compute the displacement accounting for FSI starting from the results of uncoupled simulations. The training and validation MSE loss functions over the epochs are shown in Figure 14. The mean squared error computed over the test data was 2×10^{-3}, before denormalization.

All the predictions were smoothed out using a Savitzky-

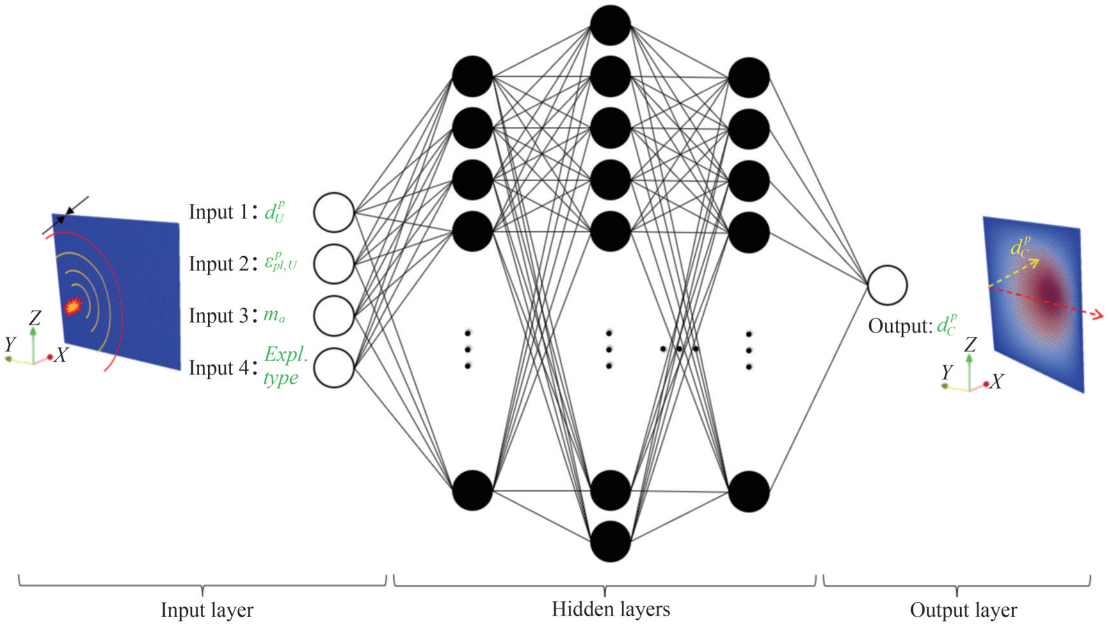

Figure 12 Schematic diagram of the DNN model of the present framework

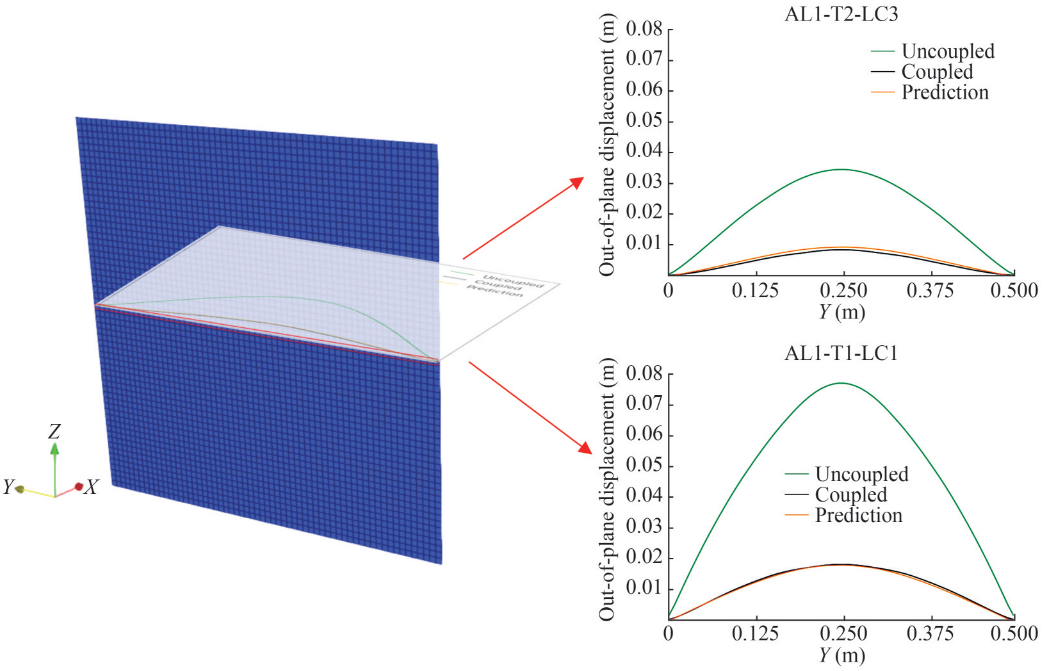

(a) Horizontal cross-section considered for the presentation of all the DNN's results

(b) Prediction of the out-of-plane displacement over the plate horizontal cross-section in two representative training scenarios

Figure 13 Example of the DNN's predictions for two representative cases of the training set

Golay filter (Luo et al., 2005), which works by fitting successive subsets of adjacent data points with a low-degree polynomial using linear least squares.

Additionally, to investigate the DNN capability of dealing with new mass-per-unit-area values, the DNN was trained on a reduced dataset including mass-per-unit-area values in the range $[21.6 \div 54.0]$ and $[125.6 \div 219.8]$. The network was then tested against new scenarios characterized by:

- Aluminum plate $-$ LC1 $-$ $s=26\,(\mathrm{mm})-m_a=70.2\,(\mathrm{kg/m^2})$;
- Aluminum plate $-$ LC2 $-$ $s=35\,(\mathrm{mm})-m_a=94.5\,(\mathrm{kg/m^2})$;
- Steel plate $-$ LC1 $-$ $s=30\,(\mathrm{mm})-m_a=235.5\,(\mathrm{kg/m^2})$.

This choice was based on the findings reported by Lomazzi et al. (2024), where m_a was identified as the driving parameter of FSI for blast-loaded plates in air.

The results are shown in Figure 16. The DNN showed extremely satisfactory generalization performance on

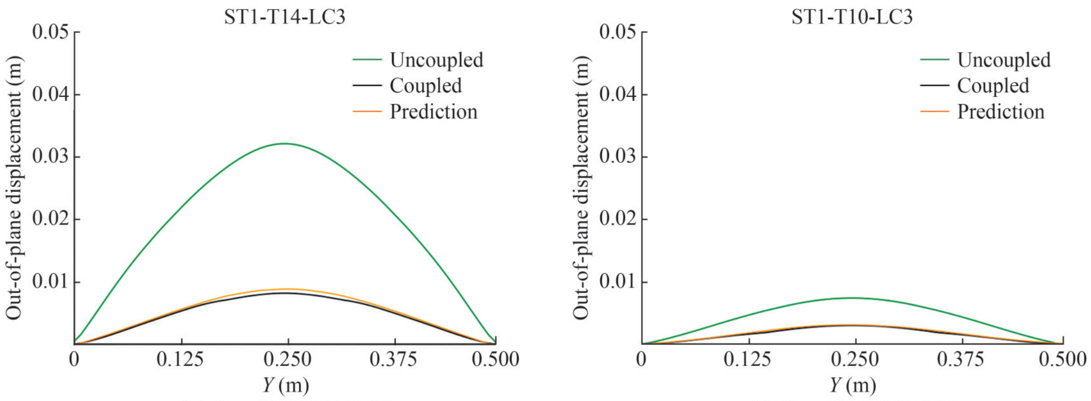

(a) Case ST1-T14-LC3 (b) Case ST1-T10-LC3

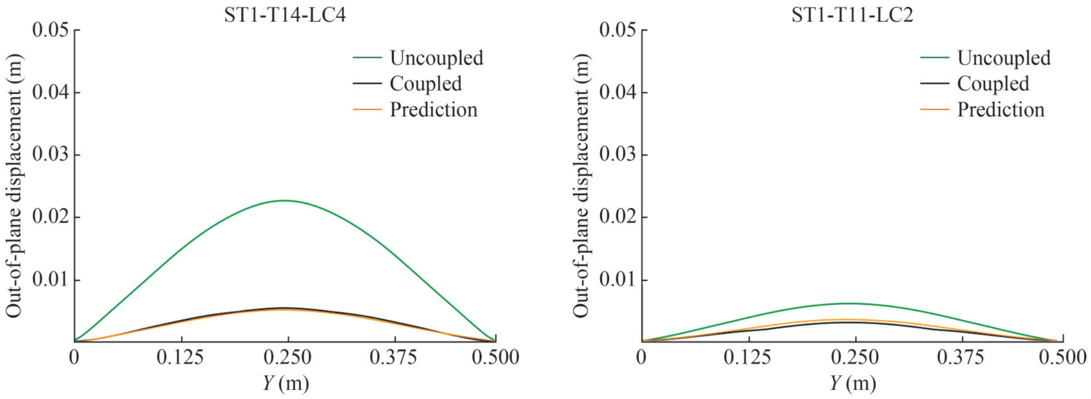

(c) Case ST1-T14-LC4 (d) Case ST1-T11-LC2

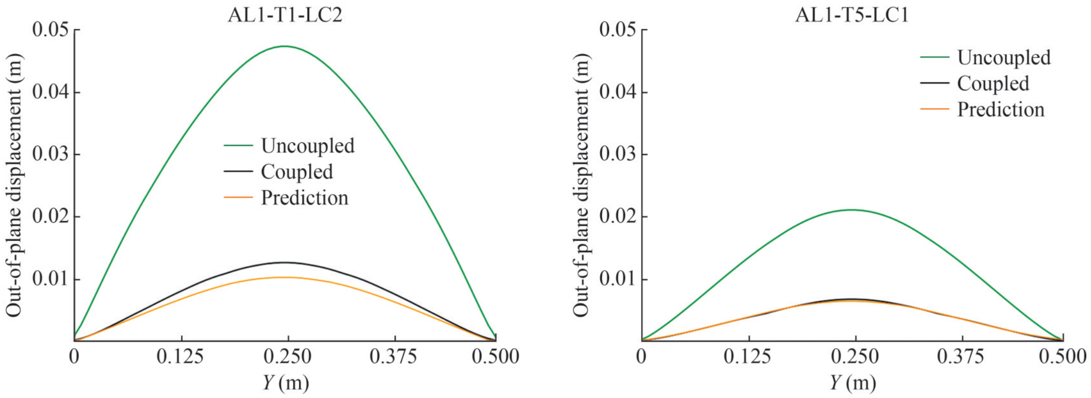

(e) Case AL1-T1-LC2 (f) Case AL1-T5-LC1

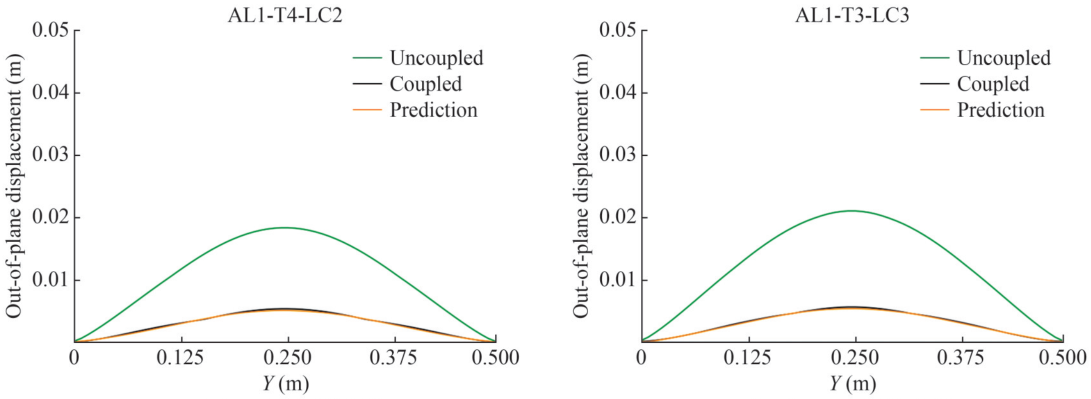

(g) Case AL1-T4-LC2 (h) Case AL1-T3-LC3

Figure 14 Prediction of the out-of-plane displacement over the horizontal cross-section in some representative test scenarios

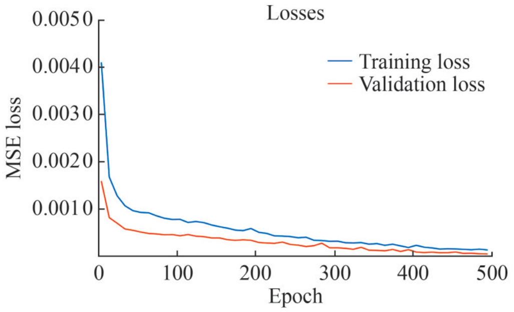

Figure 15 Mean Squared Error registered during training and validation phases

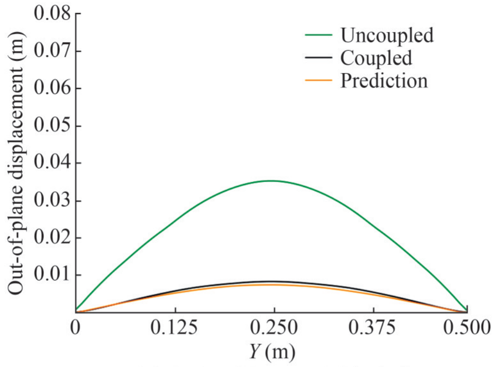

(a) AL1-LC1-$m_a = 70.2$ kg/m^2

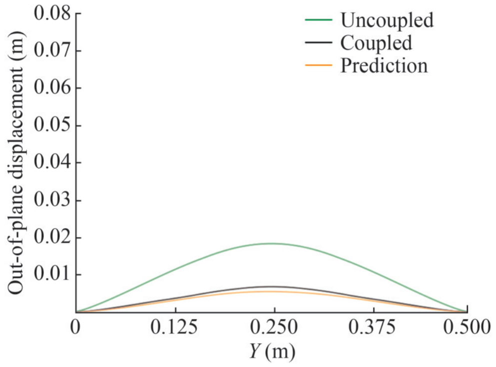

(b) AL1-LC2-$m_a = 94.5$ kg/m^2

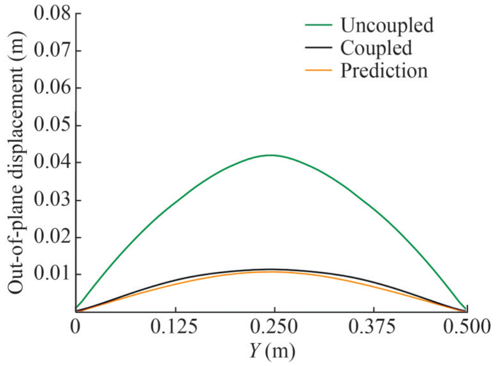

(c) ST1-LC1-$m_a = 235.5$ kg/m^2

Figure 16 Predictions of the out-of-plane displacement over the horizontal cross-section in new unseen cases

unseen mass-per-unit-area values, for both aluminum and steel plates.

Neural networks are highly sensitive to the choice of training, validation, and test splits, especially for very small datasets, where the risk of overfitting or underfitting due to improper data partitioning is significantly higher (Nguyen et al., 2019). Based on that, additional investigations were performed by the authors to demonstrate the independence of the results with respect to random splits of the dataset.

4 Conclusion and future work

This work introduces a data driven-based framework that can exploit the extreme speed of numerical simulations of UNDEX with a decoupled (or uncoupled) strategy preserving the accuracy of coupled approaches.

Uncoupled simulations, despite their great advantage related to the limited computational cost, are not able to consider the fluid-structure interaction (FSI), a non-negligible aspect in cases of explosion in an underwater environment. To overcome this, the framework calls on a machine learning strategy, i.e., a feed-forward Deep Neural Network (DNN), to learn the difference in terms of displacement field between coupled and uncoupled numerical simulations. After the training and validation phase, the neural network can take the results obtained from a decoupled analysis as input and return the displacement field that would have been obtained through a coupled analysis, avoiding making it run.

In particular, the DNN algorithm was employed to predict the maximum out-of-plane displacement contour field of submerged plates exposed to UNDEX, considering various charge masses, materials of the plate and thicknesses, starting from some features extracted from the results of uncoupled simulations. The authors verified that these valuable features are the out-of-plane displacement of the mesh element at the instant of maximum deformation, the equivalent plastic strain at the plate mid-surface at the same instant, the type of explosion and the initial mass-per-unit area of the plate.

The choice of submerged plates is due to their ability to serve as simplified models for critical structural components of ships, such as hulls, bulkheads, and decks. This simplification allows for a focused investigation of the effects of underwater explosions while maintaining relevance to real-world naval and marine engineering applications.

The DNN model was trained using data obtained from a comprehensive finite element (FE) model developed with MSC Dytran software. A total of 112 numerical simulations have been generated, consisting of 56 coupled simulations and their 56 decoupled counterparts. The problem of scarcity of numerical data available for training has been addressed by introducing augmentation processes, while the issue related to the presence of a categorical explosion type input variable was resolved by applying an embedding strategy.

The prediction of the maximum out-of-plane displacement field for all cases is in perfect agreement with the numerical (coupled) one, the latter considered with high accuracy after some experimental validations presented in the first part of the paper. Also, it's possible to highlight that since the difference between coupled and uncoupled simulations is the FSI effect, the good prediction of the deep neural network reflects an excellent ability to predict FSI, a non-trivial quantity in UNDEX, since it involves physical phenomena that are difficult to describe (e.g., cavitation, reflection phenomena, absorption, etc.).

The results of the coupled and uncoupled analyses highlight that, unlike what is observed for blast-loaded plates in air, the FSI in UNDEX scenario is significantly more intense. In fact, the uncoupled results, in terms of displacement field, are up to 300% greater than the coupled ones. As shown for plates subjected to air blasts, in this case as well, the FSI tends to reduce the structural effects (displacement field).

Overall, the advancement made in this study lies in the proposal of a tool that leverages the low computational cost of uncoupled numerical analyses to achieve accurate results. This approach extends the framework previously proposed by the same authors, which was initially applied only to air blast scenarios against plates, to now include UNDEX and marine structures.

However, the proposed framework has some limitations that should be acknowledged. First, the accuracy of the DNN heavily depends on the quality and representativeness of the numerical simulations used for training, which may limit its generalization to scenarios outside the training dataset. Second, the study simplifies the structural representation by focusing on flat plates, while real naval structures often involve stiffened panels and more complex geometries. Third, although experimental validations of the coupled analyses are presented, further experimental studies would be beneficial to confirm the framework's applicability to various conditions, including damage or failure scenarios.

Further developments of the present framework include the following aspects:

- Given that the internal behavior of the present DNN is not directly accessible without an explainability algorithm, an explainability code should be implemented in the future to elucidate the network and highlight the parameters that influence the DNN prediction process.
- Another improvement for the current framework involves applying it to scenarios where the structure exhibits damage or failure. In such cases, it would be necessary to increase the number of input parameters and account for a variable mass-per-unit area.
- The framework should be extended to submerged stiffened panels, since they are indeed commonly used in naval structures. Also, more complex floating structures and scenarios may be considered, such as the response of a hull plate in contact with water on one side and air on the other side.

Overall, it is found that the DNN has the great advantage of being accurate and rapid when predicting the maximum out-of-plane displacement of marine structures subjected to non-contact and contact UNDEX, starting from uncoupled results, considering the extremely complex fluid-structure coupling UNDEX effects, geometric and material nonlinearities.

Competing interest The authors have no competing interests to declare that are relevant to the content of this article.

References

Bardiani J, Bertagna S, Braidotti L, Marinò A, Bucci V, Sbarufatti C, Manes A (2024) Creep assessment of thermoplastic materials for non-structural components in marine engines. Compos Part B Eng 287: 111800. https://doi.org/10.1016/j.compositesb.2023.111800

Bardiani J, Sbarufatti C, Manes A (2025) Transfer learning with deep neural network toward the prediction of the mass of the charge in underwater explosion events. J Mar Sci Eng 13(2): 190. https://doi.org/10.3390/jmse13020190

Biglarkhani M, Sadeghi K (2017) Incremental explosive analysis and its application to performance-based assessment of stiffened and unstiffened cylindrical shells subjected to underwater explosion. Shock Vib 2017(1): 3754510. https://doi.org/10.1155/2017/3754510

Bousmaha R, Hamou RM, Amine A (2022) Automatic selection of hidden neurons and weights in neural networks for data classification using hybrid particle swarm optimization, multi-verse optimization based on Lévy flight. Evol Intell 15(3): 1695-1714. https://doi.org/10.1007/s12065-021-00579-w

Brunton SL, Noack BR, Koumoutsakos P (2020) Machine learning for fluid mechanics. Annu Rev Fluid Mech 52(1): 477-508. https://doi.org/10.1146/annurev-fluid-010719-060214

Cole RH (1948) Underwater explosions. Princeton University Press

Cui P, Zhang AM, Wang SP (2016) Small-charge underwater explosion bubble experiments under various boundary conditions. Phys Fluids 28(11): 117101. https://doi.org/10.1063/1.4967700

De Camargo FV (2019) Survey on experimental and numerical approaches to model underwater explosions. J Mar Sci Eng. https://doi.org/10.3390/jmse7010015

Ding P, Buijk A (2006) Simulation of underwater explosion using MSC Dytran. Ann Arbor 1001: 48105

DNV GL (2015) CLASS GUIDELINE Finite element analysis. DNV GL

Elkaseer A, Abdelaziz A, Saber M, Nassef A (2019) FEM-based study of precision hard turning of stainless steel 316L. Materials 12(16): 2522. https://doi.org/10.3390/ma12162522

Flores-Johnson EA, Shen L, Guiamatsia I, Nguyen GD (2014) Numerical investigation of the impact behaviour of bioinspired nacre-like aluminium composite plates. Compos Sci Technol 96: 13-22. https://doi.org/10.1016/j.compscitech.2014.03.001

Ge L, Zhang AM, Wang SP (2020) Investigation of underwater explosion near composite structures using a combined RKDG-FEM approach. J Comput Phys 404: 109113. https://doi.org/

10.1016/j.jcp.2019.109113

Giuliano D, Lomazzi L, Giglio M, Manes A (2023) On Eulerian-Lagrangian methods to investigate the blast response of composite plates. Int J Impact Eng 173: 104469. https://doi.org/10.1016/j.ijimpeng.2022.104469

Hastie T, Tibshirani R, Friedman J (2009) Springer series in statistics: the elements of statistical learning. Math Intell 27(2): 83-85. https://doi.org/10.1007/b94608

Hinton GE, Osindero S, Teh YW (2006) A fast learning algorithm for deep belief nets. Neural Comput 18(7): 1527-1554. https://doi.org/10.1162/neco.2006.18.7.1527

Huang H, Jiao QJ, Nie JX, Qin JF (2011) Numerical modeling of underwater explosion by one-dimensional ANSYS-AUTODYN. J Energetic Mater 29(4): 292-325. https://doi.org/10.1080/07370652.2010.527898

Jha N, Kumar BK (2014) Underwater explosion pressure prediction and validation using ANSYS/AUTODYN. Int J Sci Res 3(12): 1162-1166

Jin QK, Ding GY (2011) A finite element analysis of ship sections subjected to underwater explosion. Int J Impact Eng 38(7): 558-566. https://doi.org/10.1016/j.ijimpeng.2010.11.005

Keil AH (1961) The response of ships to underwater explosion. SNAME 69: 366-410

Kiciński R, Szturomski B (2020) Pressure wave caused by trinitrotoluene (TNT) underwater explosion—short review. Appl Sci 10(10): 3433. https://doi.org/10.3390/app10103433

Kong XS, Gao H, Jin Z, Zheng C, Wang Y (2023) Predictions of the responses of stiffened plates subjected to underwater explosion based on machine learning. Ocean Eng 283: 115216. https://doi.org/10.1016/j.oceaneng.2023.115216

Kumar L, Tummalapalli S, Rathi SC, Murthy LB, Krishna A, Misra S (2023) Machine learning with word embedding for detecting web-services anti-patterns. J Comput Lang 75: 101207. https://doi.org/10.1016/j.cola.2023.101207

Kwon YW, Fox PK (1993) Underwater shock response of a cylinder subjected to a side-on explosion. Comput Struct 48(4): 637-646. https://doi.org/10.1016/0045-7949(93)90056-X

Lee T, Kwak BJ, Yu J, Lee JH, Noh Y, Moon YH (2020) Deep-learning approach to predict a severe plastic anisotropy of caliber-rolled Mg alloy. Mater Lett 269: 127652. https://doi.org/10.1016/j.matlet.2020.127652

Lee YJ, Hsu CH, Huang CH (2008) Pressure hull analysis under shock loading. Shock Vib 15(1): 19-32. https://doi.org/10.1155/2008/851290

Liu WT, Ming FR, Zhang AM, Miao XH, Liu YL (2018) Continuous simulation of the whole process of underwater explosion based on Eulerian finite element approach. Appl Ocean Res 80: 125-135. https://doi.org/10.1016/j.apor.2018.08.016

Liu Y, Li Z, Sun Q, Fan X, Wang W (2013) Separation dynamics of large-scale fairing section: A fluid–structure interaction study. Proc Inst Mech Eng G J Aerosp Eng 227(11): 1767-1779. https://doi.org/10.1177/0954410012462317

Liu YZ, Ren SF, Zhao PF (2022) Application of the deep neural network to predict dynamic responses of stiffened plates subjected to near-field underwater explosion. Ocean Eng 247: 110537. https://doi.org/10.1016/j.oceaneng.2022.110537

Löhner R, Li L, Soto OA, Baum JD (2023) An arbitrary Lagrangian–Eulerian method for fluid−structure interactions due to underwater explosions. Int J Numer Methods Heat Fluid Flow 33(6): 2308-2349. https://doi.org/10.1108/HFF-08-2022-0502

Lomazzi L, Morin D, Cadini F, Manes A, Aune V (2024) Deep learning-based analysis to identify fluid-structure interaction effects during the response of blast-loaded plates. Int J Protect Struct 15(4): 722-752. https://doi.org/10.1177/20414196231198259

Luo J, Ying K, He P, Bai J (2005) Properties of Savitzky–Golay digital differentiators. Digit Signal Process 15(2): 122-136. https://doi.org/10.1016/j.dsp.2004.09.008

Ming FR, Zhang AM, Xue YZ, Wang SP (2016) Damage characteristics of ship structures subjected to shockwaves of underwater contact explosions. Ocean Eng 117: 359-382. https://doi.org/10.1016/j.oceaneng.2016.03.040

Mumuni A, Mumuni F (2022) Data augmentation: A comprehensive survey of modern approaches. Array 16: 100258. https://doi.org/10.1016/j.array.2022.100258

Murugesan M, Jung DW (2019) Johnson Cook material and failure model parameters estimation of AISI-1045 medium carbon steel for metal forming applications. Materials 12(4): 609. https://doi.org/10.3390/ma12040609

Nayak S, Lyngdoh GA, Shukla A, Das S (2022) Predicting the near field underwater explosion response of coated composite cylinders using multiscale simulations, experiments, and machine learning. Compos Struct 283: 115157. https://doi.org/10.1016/j.compstruct.2021.115157

Neto LB, Saleh M, Pickerd V, Yiannakopoulos G, Mathys Z, Reid W (2020) Rapid mechanical evaluation of quadrangular steel plates subjected to localised blast loadings. Int J Impact Eng 137: 103461. https://doi.org/10.1016/j.ijimpeng.2019.103461

Nguyen AT (2023) A numerical research on the interaction between underwater explosion bubble and deformable structure using CEL technique. EUREKA: Phys Eng 2023(1): 134-151. https://doi.org/10.21303/2461-4262.2023.002637

Nguyen G, Dlugolinsky S, Bobák M, Tran V, López García Á, Heredia I, Hluchý L (2019) Machine learning and deep learning frameworks and libraries for large-scale data mining: a survey. Artif Intell Rev 52: 77-124. https://doi.org/10.1007/s10462-018-09679-z

Nguyen VT, Phan TH, Duy TN, Park WG (2021) Numerical modeling for compressible two-phase flows and application to near-field underwater explosions. Comput Fluids 215: 104805. https://doi.org/10.1016/j.compfluid.2020.104805

Olmi F, Nascimento KD (1999) Small debris impact simulation using MSC/DYTRAN. In: 1999 MSC Worldwide Aerospace Conference Proceedings, Vol. 1

Peng YX, Zhang AM, Ming FR (2021) Numerical simulation of structural damage subjected to the near-field underwater explosion based on SPH and RKPM. Ocean Eng 222: 108576. https://doi.org/10.1016/j.oceaneng.2021.108576

Rackwitz F (2020) Possibilities and limitations of ALE large deformations analyses in geotechnical engineering. In: Recent Developments of Soil Mechanics and Geotechnics in Theory and Practice, pp. 97-112. Springer International Publishing. https://doi.org/10.1007/978-3-030-51211-1_8

Rajendran R, Narasimhan K (2001) Damage prediction of clamped circular plates subjected to contact underwater explosion. Int J Impact Eng 25(4): 373-386. https://doi.org/10.1016/S0734-743X(00)00054-5

Ramajeyathilagam K, Vendhan CP (2004) Deformation and rupture of thin rectangular plates subjected to underwater shock. Int J Impact Eng 30(6): 699-719. https://doi.org/10.1016/j.ijimpeng.2003.01.001

Ren SF, Zhao PF, Wang SP, Liu YZ (2022) Damage prediction of stiffened plates subjected to underwater contact explosion using the machine learning-based method. Ocean Eng 266: 112839. https://doi.org/10.1016/j.oceaneng.2022.112839

Rolfe E, Quinn R, Irven G, Brick D, Dear JP, Arora H (2020) Underwater blast loading of partially submerged sandwich composite materials in relation to air blast loading response. Int J Lightweight Mater Manuf 3(4): 387-402. https://doi.org/10.1016/j.ijlmm.2020.06.003

Sagar HJ, El Moctar O (2023) Dynamics of a cavitation bubble between oblique plates. Phys Fluids 35(1): 017105. https://doi.org/10.1063/5.0132098

Sagar HJ, el Moctar O (2024) Hydroelasticity effects induced by a single cavitation bubble collapse. J Fluids Struct 127: 104131. https://doi.org/10.1016/j.jfluidstructs.2024.104131

Shehu E, Lomazzi L, Giglio M, Manes A (2023) Computational modeling of confined blast waves with focus on interaction with structures. In: IOP Conf Ser Mater Sci Eng 1275(1): 012028. https://doi.org/10.1088/1757-899X/1275/1/012028

Sigrist JF, Broc D (2023) A versatile method to calculate the response of equipment mounted on ship hulls subjected to underwater shock waves. Finite Elem Anal Des 218: 103917. https://doi.org/10.1016/j.finel.2023.103917

Spear DG, Palazotto AN, Kemnitz RA (2021) Modeling and simulation techniques used in high strain rate projectile impact. Mathematics 9(3): 274. https://doi.org/10.3390/math9030274

Tran P, Wu C, Saleh M, Neto LB, Nguyen-Xuan H, Ferreira AJM (2021) Composite structures subjected to underwater explosive loadings: A comprehensive review. Compos Struct 263: 113684. https://doi.org/10.1016/j.compstruct.2021.113684

Venkatesan J, Iqbal MA, Gupta NK, Bratov V, Kazarinov N, Morozov F (2017) Ballistic characteristics of bi-layered armour with various aluminium backing against ogive nose projectile. Procedia Struct Integr 6: 40-47. https://doi.org/10.1016/j.prostr.2017.11.007

Walters AP, Didoszak JM, Kwon YW (2013) Explicit modeling of solid ocean floor in shallow underwater explosions. Shock Vib 20(1): 189-197. https://doi.org/10.3233/SAV-2012-0737

Wang H, Cheng YS, Liu J, Gan L (2016) The fluid-solid interaction dynamics between underwater explosion bubble and corrugated sandwich plate. Shock Vib 2016(1): 6057437. https://doi.org/10.1155/2016/6057437

Wang H, Liu B, Lei J, Zhao N (2024) Improved deep neural network for predicting structural response of stiffened cylindrical shells to far-field underwater explosion. Ocean Eng 298: 117258. https://doi.org/10.1016/j.oceaneng.2024.117258

Wang Y, Dong H, Dong T, Xu X (2022) Dumbbell-shaped damage effect of closed cylindrical shell subjected to far-field side-on underwater explosion shock wave. J Mar Sci Eng 10(12): 1874. https://doi.org/10.3390/jmse10121874

Yu J, Liu JH, Wang HK, Wang J, Zhou ZT, Mao HB (2022) Application of two-phase transition model in underwater explosion cavitation based on compressible multiphase flows. AIP Adv 12(2): 025117. https://doi.org/10.1063/5.0077517

Zhang ZF, Wang C, Wang LK, Zhang AM, Silberschmidt VV (2018) Underwater explosion of cylindrical charge near plates: Analysis of pressure characteristics and cavitation effects. Int J Impact Eng 121: 91-105. https://doi.org/10.1016/j.ijimpeng.2018.06.009

Zhou ZH (2021) Machine learning. Springer nature. https://doi.org/10.1007/978-981-15-1967-3